Discovery of thermonuclear (Type I) X-ray bursts in the X-ray binary Swift J1858.6–0814 observed with *NICER* and *NuSTAR*

D. J. K. Buisson,[1]★ D. Altamirano,[1] P. Bult,[2,3] G. C. Mancuso,[4,5] T. Güver,[6,7] G. K. Jaisawal [8] J. Hare,[3]†
A. C. Albayati [1] Z. Arzoumanian,[3] N. Castro Segura [1] D. Chakrabarty,[9] P. Gandhi [1] S. Guillot [10]
J. Homan,[11,12] K. C. Gendreau,[3] J. Jiang [13,14] C. Malacaria [15,16]† J. M. Miller,[17] M. Özbey Arabacı,[1,18]
R. Remillard,[9] T. E. Strohmayer,[19] F. Tombesi,[2,3,20,21] J. A. Tomsick,[22] F. M. Vincentelli [1]
and D. J. Walton [23]

Affiliations are listed at the end of the paper

ABSTRACT

Swift J1858.6–0814 is a recently discovered X-ray binary notable for extremely strong variability (by factors of >100 in soft X-rays) in its discovery state. We present the detection of five thermonuclear (Type I) X-ray bursts from Swift J1858.6–0814, implying that the compact object in the system is a neutron star (NS). Some of the bursts show photospheric radius expansion, so their peak flux can be used to estimate the distance to the system. The peak luminosity, and hence distance, can depend on several system parameters; for the most likely values, a high inclination and a helium atmosphere, $D = 12.8^{+0.8}_{-0.6}$ kpc, although systematic effects allow a conservative range of 9–18 kpc. Before one burst, we detect a QPO at 9.6 ± 0.5 mHz with a fractional rms amplitude of 2.2 ± 0.2 per cent (0.5–10 keV), likely due to marginally stable burning of helium; similar oscillations may be present before the other bursts but the light curves are not long enough to allow their detection. We also search for burst oscillations but do not detect any, with an upper limit in the best case of 15 per cent fractional amplitude (over 1–8 keV). Finally, we discuss the implications of the NS accretor and this distance on other inferences which have been made about the system. In particular, we find that Swift J1858.6–0814 was observed at super-Eddington luminosities at least during bright flares during the variable stage of its outburst.

Key words: accretion, accretion discs – stars: neutron – X-rays: binaries – X-rays: bursts.

1 INTRODUCTION

A key aspect of accreting systems is the object on to which the accretion is occurring; in X-ray binaries (XRBs), this is either a neutron star (NS) or black hole (BH). Many observable properties are similar in either case, so determining which is present is often a challenging task.

There are several properties, which can divide NSs and BHs as populations and some features, which empirically appear to occur in only one type of system. First, outbursts of the different classes of source follow different tracks in gross properties such as the hardness–intensity or colour–colour diagrams (e.g. van der Klis 2006). However, this requires monitoring of the full outburst and some sources do not follow the typical patterns. Additionally, quasiperiodic oscillations (QPOs) are only found at kHz frequencies in NS systems (Strohmayer et al. 1996; van der Klis et al. 1996), although there is not yet a universally accepted model for their production (e.g. review by van der Klis 2006).

Also, BH and NS systems can be separated in the radio/X-ray luminosity plane (while in the hard state), with BH systems being

radio brighter (Migliari & Fender 2006; Gallo, Degenaar & van den Eijnden 2018). Similarly, the hard Comptonized component tends to have a higher temperature in BH systems (Burke, Gilfanov & Sunyaev 2017). However, the loci of BHs and NSs overlap in these properties, so they cannot be used to determine the accretor definitively in an individual source, particularly where a source shows unusual properties.

Other properties of an accreting system can give a definitive determination of whether the accreting object is a BH or an NS. To confirm a BH accretor requires a dynamical mass measurement, which is greater than possible NS masses (e.g. Bolton 1972; Webster & Murdin 1972; Orosz & Bailyn 1997), since there are no particular accretion properties, which are unique to BHs. Conversely, there are several properties, which are confirmed as unique to NSs, since the NS surface can provide an additional location for emission components and they can support large-scale magnetic fields. The emission from this surface may be detected directly as a soft (0.1–0.3 keV) blackbody-like component (e.g. Brown, Bildsten & Rutledge 1998). This component is much fainter than the accretion luminosity, so cannot be identified during the first outburst in which a source is detected and requires sensitive observations to detect. Also, NSs can pulse coherently on their spin period, which can be observed at wavelengths from radio (Hewish et al. 1968) to X-ray (e.g. review by Patruno & Watts 2012). A further feature of XRBs

★ E-mail: d.j.k.buisson@soton.ac.uk
† NASA Postdoctoral Fellow.

particular to those hosting NSs is Type I X-ray bursts (e.g. Grindlay et al. 1976; Hoffman, Marshall & Lewin 1978; Lewin, van Paradijs & Taam 1993; Strohmayer & Bildsten 2006; Galloway et al. 2008a; Galloway & Keek 2017).

Type I X-ray bursts occur due to explosive thermonuclear burning of accreted material on the NS surface. As material accretes on to the NS, it adds to layers of hydrogen and helium on the surface. When the pressure at the bases of these layers becomes large enough, it will ignite thermonuclear burning. Depending on the conditions, this burning may occur stably, contributing to the power in the persistent emission, or explosively, producing Type I bursts. These bursts can be ignited by hydrogen and/or helium (or occasionally carbon in 'superbursts', e.g. Cornelisse et al. 2000; Cumming & Bildsten 2001; Strohmayer & Brown 2002; in't Zand 2017), depending on the stability of each burning process, which depends principally on the accretion rate (Narayan & Heyl 2003) but also the metallicity of the accreted material and the internal temperature of the NS (Bildsten 1995, 1998; Cumming & Macbeth 2004). The basic classes of burning are thought to be as follows: While these classes of burning are reproduced in most numerical studies of Type I bursts, the exact values of accretion rate at which each one occurs differ between works (e.g. Fujimoto, Hanawa & Miyaji 1981; Bildsten 1998; Narayan & Heyl 2003).

At low accretion rates, a layer of hydrogen builds up before it reaches sufficient pressure to begin burning. At this point, the energy released by ignition causes most of the hydrogen layer to burn rapidly, which is observed as a Type I burst. At higher accretion rates, the accreted hydrogen promptly reaches sufficient temperature and pressure to burn so the burning is stable. When sufficient helium builds up, the pressure ignites helium burning, which is responsible for the burst. At still higher accretion rates, not all of the hydrogen can be burnt before helium ignition occurs; this hydrogen is burnt along with the helium in a mixed burst. At the highest accretion rates, both hydrogen and helium burning occur stably so no Type I bursts are observed. However, close to the transition to stability, the burning is marginally stable and has an oscillatory mode (Heger, Cumming & Woosley 2007), which has been used to explain the millihertz (mHz) QPOs observed prior to some Type I bursts (Revnivtsev et al. 2001; Altamirano et al. 2008; Lyu et al. 2016; Mancuso et al. 2019).

There are also other effects, which can affect the occurrence and type (fuel) of thermonuclear bursts. Each burst may not burn all of the available fuel, so some hydrogen and helium will remain after one burst and can affect properties of following bursts. Similarly, the burnt material will contain additional carbon, nitrogen, and oxygen from helium burning. These nuclei catalyse hydrogen burning so can affect later bursts as well. The NS spin (Spitkovsky, Levin & Ushomirsky 2002; Galloway et al. 2018) and the geometry of where on the star the material is accreted (Kajava et al. 2014) can also affect burst properties.

Type I bursts can sometimes be used as standard candles, as they can be bright enough to reach the Eddington limit. In this situation, the radiation pressure lifts material in the NS surface and the atmosphere expands in photospheric radius expansion (PRE; Lewin, Vacca & Basinska 1984; Tawara et al. 1984). Since the Eddington limit is only weakly dependent on radius, this produces a period during which the luminosity remains constant at the (known) Eddington value. This PRE phase may be identified (and distinguished from a simple plateau in the burning rate) by measuring the change in photospheric radius from the time-resolved X-ray spectrum. The measured flux during the PRE phase may then be used with this standard candle to estimate the distance to the source (van Paradijs 1978; Kuulkers et al. 2003).

1.1 Swift J1858.6–0814

The low-mass X-ray binary Swift J1858.6–0814 has been in its first observed outburst since late 2018 (Krimm et al. 2018). The X-ray emission in the initial phase of the outburst was highly variable as was the emission in other wavebands (Fogantini et al., in preparation; Ludlam et al. 2018; van den Eijnden et al. 2020): the *NICER* 0.5–10 keV count rate peaks at over 650 count s^{-1} within 200 s of intervals at ≈2.5 count s^{-1} (Fogantini et al., in preparation), much larger than the typical tens of per cent RMS on these time-scales (McClintock & Remillard 2006). We refer to this stage of the outburst (all observations in 2018 and 2019) as the flaring state. The X-ray spectra were also extremely hard: $\Gamma < 1$ if fitted with a simple power law, (Kennea & Krimm 2018; Ludlam et al. 2018), compared to typical $\Gamma > 1.5$ (e.g. Zdziarski, Lubiński & Smith 1999). This may be explained by the contribution of reflection and absorption: they also show a strong neutral iron Kα line and K edge (Reynolds et al. 2018; Hare et al. 2020) and soft X-ray emission lines (Buisson et al. 2020a). It also shows P-Cygni lines in its optical spectra, which look similar to those seen in several BH XRBs (Castro-Segura, in preparation; Munoz-Darias et al. 2019; Muñoz-Darias et al. 2020), as well as strongly variable optical emission (Paice et al. 2018). These properties have led to Swift J1858.6–0814 being viewed (Hare et al. 2020) as an analogue of V404 Cyg (Gandhi et al. 2016; Motta et al. 2017; Walton et al. 2017) and V4641 Sgr (Wijnands & van der Klis 2000; Revnivtsev et al. 2002), which have been dynamically confirmed as hosting BHs (Casares, Charles & Naylor 1992; Orosz et al. 2001, respectively). Swift J1858.6–0814 also lies within the range occupied by BHs in the radio-X-ray plane (van den Eijnden et al. 2020). However, recent observations of Swift J1858.6–0814 have shown qualitatively different X-ray properties, suggesting a state change while the source was unobservable due to Sun constraint (between 2019 November and 2020 February), although the properties of the initial phase were not typical of a canonical state (e.g. van der Klis 1994). In the 2020 observations, the flux level is much steadier and the strong iron line and edge are absent (and fig. 1 of Buisson et al. 2020b),. These observations have also shown Type I X-ray bursts in both *NICER* and *NuSTAR* data (Buisson et al. 2020c), unambiguously identifying the compact object as an NS.

In this paper, we analyse the Type I X-ray bursts detected in *NICER* and *NuSTAR* data of Swift J1858.6–0814.

2 OBSERVATIONS AND DATA REDUCTION

We have inspected the *NICER* (Gendreau et al. 2016) light curves from 2020 by eye. Apparent Type I bursts are present in OB-SIDs 3200400106, 3200400111, 3200400114, 3200400121, and 3200400122, corresponding to March 6, 11, 14, 21, and 22.

We begin with the calibrated, unfiltered events file from HEASARC (`event_cl/ni32004001**_0mpu7_ufa.evt`). We use the standard filters[1] to produce good time intervals apart from the undershoot range, which we relax from $\leq$200 to $\leq$300 s^{-1} for the first Type I burst and $\leq$250 s^{-1} for the second. This is required due to high optical loading due to the relatively low Sun angle. Additionally, to include the peak of the second burst, we relax the offset from the nominal target direction slightly, using 0.0155° rather than 0.015°. This is a small change from the standard value, so data during this time are unlikely to show significant deviations from the standard calibration. Further, the fourth burst

[1]For further information on the filters, see heasarc.gsfc.nasa.gov/lheasoft/ftools/headas/nimaketime.html.
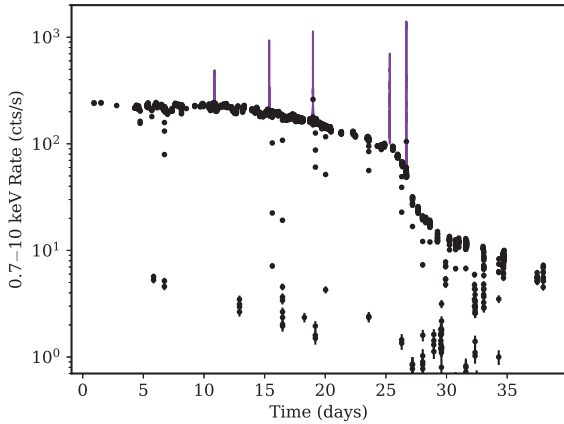
Figure 1. *NICER* light curve of Swift J1858.6–0814 since leaving Sun constraint in 2020, showing times of observed Type I bursts (purple). In addition to the long-term flux decrease, several dips, and eclipses are visible; these will be considered in detail in future work. The full *NICER* light curve is shown in black at a resolution of 40 s and the bursts (purple) extend to their maximum count rate at 0.1 s resolution. The zero-point for the time axis is the start of 2020 February 25 (MJD 58904).

occurs during passage through the South Atlantic Anomaly (SAA) and the overshoot rate reaches close to $5\,s^{-1}$, so is removed by standard filtering. We remove these filters in order to show the light curve but note that the spectrum may be affected.

We then use NICERCLEAN to produce a clean events list, which we then barycentre to the ICRS reference frame and JPL-DE200 ephemeris. From this, we extract spectra and light curves using XSELECT.

We use *NuSTAR* (Harrison et al. 2013) OBSID 90601308002, which overlaps with *NICER* OBSID 3200400106. We reduce this using the standard NUPIPELINE and NUPRODUCTS software, version 1.9.0. We use a source region of a circle of radius 2 arcmin centred on the centroid of the detected counts. We use a background region of a circle of radius 2 arcmin from a source-free area of the detector.

3 RESULTS AND DISCUSSION

3.1 Long-term light curve and burst recurrence time

We show the light curve of Swift J1858.6–0814 since leaving Sun constraint on 2020 February 25 in Fig. 1. The count rate shows a secular decrease throughout the whole of this period, punctuated by short dips and eclipses as well as the five Type I bursts analysed here. The drop in persistent count rate from the first to the last burst was by a factor of around 4 and bursts were, in general, brighter at lower persistent count rate, with only the fourth burst not following this trend. Around the time of the last observed burst, the rate started decreasing more rapidly, before flattening once more. The period of fastest flux drop extended considerably before and after the final burst, so the coincidence in time is probably only by chance. As well as the Type I bursts, several dips are present, many of which are due to eclipses (Buisson et al. 2020c); these will be analysed in detail in future work.

The times between Type I bursts are 4.5, 3.6, 6.3, and 1.4 d (we summarize lists, such as this, of properties of each burst in Table A1). Since the coverage of Swift J1858.6–0814 is not continuous, there may have been other bursts between those observed, in observation gaps. Therefore, these gaps are an upper limit to the recurrence time. The duty cycle of *NICER* observations is low ($\approx$3.9 per cent over

the 37 d shown in Fig. 1, but not evenly across this time) so it is very likely that other bursts did occur outside times of observation. Furthermore, we can consider the α-value, the ratio of inter-burst (persistent) fluence to burst fluence, which is typically $\approx$40 for hydrogen-fuelled bursts and $\approx$100–200 for helium (e.g. Gottwald et al. 1986; Galloway et al. 2004). Here, the lowest observed α $\approx$ 500 (for burst 5, integrating the fluxes found in Section 3.4) is higher, meaning more emission occurs between bursts than would be expected. This suggests that other, intermediate bursts did occur and/or substantial nuclear burning occurred between bursts.

There is also a period longer than any gap between observed bursts at the start of the *NICER* monitoring ($\approx$10 d) where no bursts are observed; again, it is possible that bursts did occur during this period but that they occurred during gaps in the *NICER* monitoring (which observed only 0.24 d of this time). The count rate and spectral shape show no large changes during this time, so there is no obvious reason for bursts not to have occurred. An alternative explanation for the lack of bursts in this period is that it followed a superburst, which quenched the normal Type I bursts (Keek, Heger & in't Zand 2012); however, there is no evidence in the *NICER* monitoring or *MAXI* data (which cover earlier times) for a superburst having occurred.

3.2 Confirmation of source of Type I bursts

The first burst was observed by both *NuSTAR* and *NICER*. We show a *NuSTAR* image of the sky around Swift J1858.6–0814 in Fig. 2. This shows that, to the resolution available to *NuSTAR*, only one source is apparent in the *NICER* field of view and the location of the Type I burst flux is consistent with the location of the persistent emission. The offset between the *NuSTAR* position and the nominal *NICER* pointing is around 15 arcsec, which is less than the 1 arcmin nominal pointing stability of *NICER* (Arzoumanian et al. 2014). This shows that the X-ray bursts are from Swift J1858.6–0814.

3.3 Type I X-ray burst light curves

The light curves for each Type I burst are shown in Fig. 3. Each burst has a fast rise, lasting $\lesssim$3 s, a single peak and fades to being undetectable over the persistent level within up to $\approx$40 s. The decay of each burst, except the first, has an initial fast drop (within $\approx$2–3 s of the peak) followed by a slower exponential fade, lasting the remainder of the time (up to $\approx$40 s) when the burst is observable over the persistent flux. This fast drop is by a greater factor in brighter bursts (Fig. 4); for example, this drop is by a factor of $\approx$2.5 in burst 1 but $\approx$4 in burst 4. This shape is typical of Type I bursts fuelled by helium (Galloway et al. 2008a). Helium fuelled bursts can arise either when the accreted fuel is hydrogen poor or when accreted hydrogen burns stably between bursts; the binary orbital period is too long ($\approx$76840 s, Buisson et al. 2020c) for a helium white dwarf companion and hydrogen is present in the optical spectra of the accretion disc/wind (Muñoz-Darias et al. 2020) so the latter case is more likely. The upper limits on the burst recurrence time (1.4 d in the best case) are long enough that sufficient hydrogen burning is plausible. The first burst is considerably fainter (peaking at $\approx$290 count s^{-1} over 0.5–10 keV; the next faintest, burst 4, peaks at $\approx$600 count s^{-1}) and shorter than the others. Apart from the fourth, each burst is stronger than the previous one, while the persistent count rate decreases; this could be due to partial burning of the accreted material occurring outside bursts producing more H-poor fuel in the latter bursts, if more inter-burst burning occurred due to a longer recurrence time.
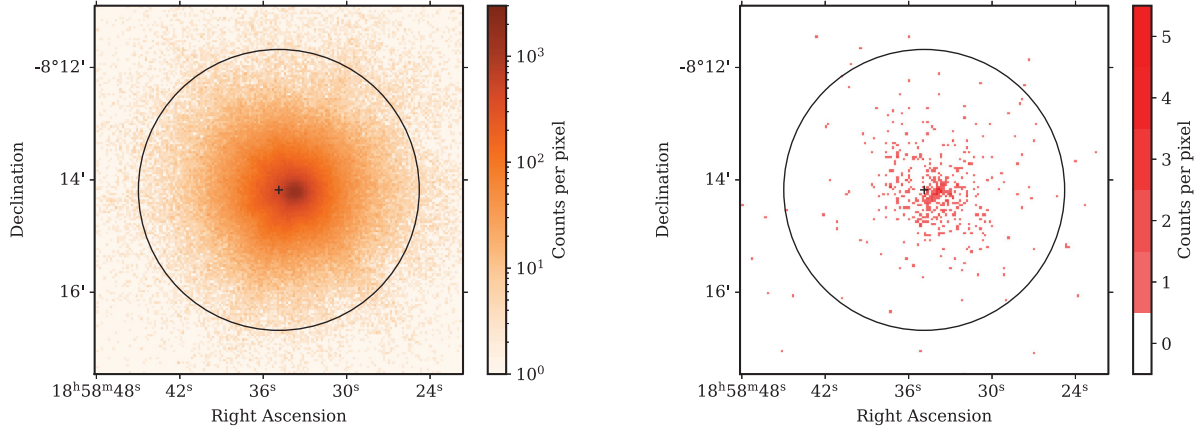
Figure 2. 3–50 keV *NuSTAR* image of the sky around Swift J1858.6–0814. Left-hand panel: over the full (26.7 ks on source time) observation; only a single point source is apparent, at the position of Swift J1858.6–0814. Right-hand panel: during the Type I burst only; the source position matches the position during the full observation. The *NICER* field of view is shown by the black circle and the nominal pointing direction by the black cross.
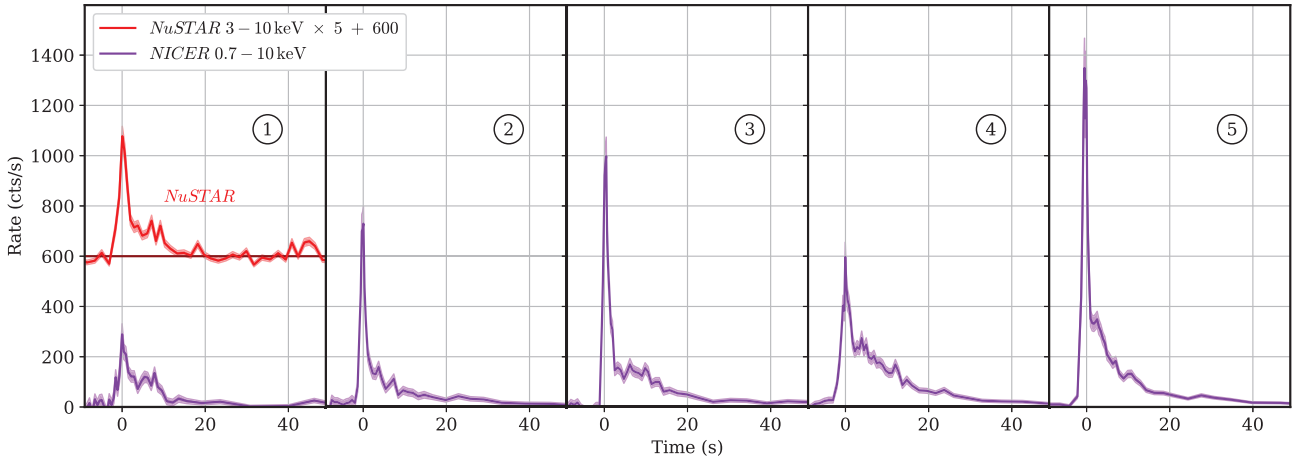

Figure 3. Light curves of each Type I burst, in order of occurrence. Purple: 0.7–10 keV *NICER*; red: 3–10 keV *NuSTAR*, scaled (increased by a factor of 5) and offset (by +600 count s^{-1}). Each burst has had the persistent rate (the mean rate from 50–200 s before the burst) subtracted. The shaded regions are the 1σ Poisson uncertainties.
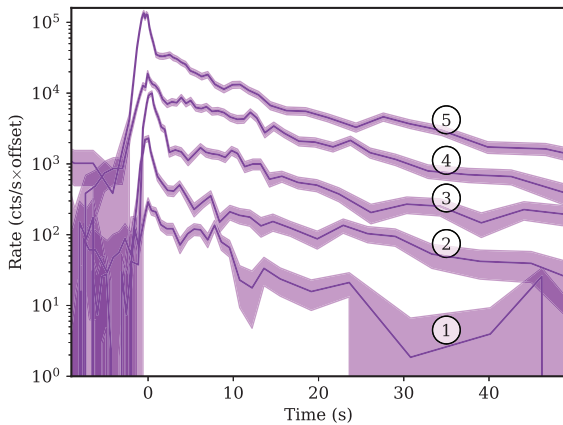

Figure 4. Light curves of each Type I burst, in order of occurrence from the bottom to top. Purple: 0.7–10 keV *NICER*. Each burst is offset from the previous by a factor of $10^{0.5}$. Each burst has had the persistent rate (the mean rate from 50–200 s before the burst) subtracted. The cooling tail is similar for each burst but bursts 2, 3, and 5 have a stronger initial peak. The shaded regions are the 1σ Poisson uncertainties.

3.4 Time-resolved spectroscopy

We extract time-resolved spectra for each Type I burst using time intervals containing a minimum number of photons. First, we estimate the persistent emission from the interval from 200 to 50 s before the burst peak. We then define the start of the burst: we take a light curve binned to 0.1 s and find the final bin before the burst which is not above the persistent rate. We define the burst as starting at the end of this bin. Starting from this point, we extract spectra from time intervals containing at least 300 counts in excess of that expected from the persistent rate. We then fit the spectrum of the burst emission as the difference between each burst spectrum and the persistent spectrum (this is performed by treating the persistent emission as the background). We initially model the burst emission with a single blackbody. Apart from around the burst peaks, the spectra are described well by this model. However, spectra around the peaks of the second, third, and fifth bursts are broader than a simple blackbody and in the fits show excess emission at low energies. We test two alternative phenomenological models to explain this excess: allowing the normalization of the persistent emission to change by a factor $(1 + f_a)$ (Worpel, Galloway & Price 2013) or adding a second blackbody. The former case requires a model for the
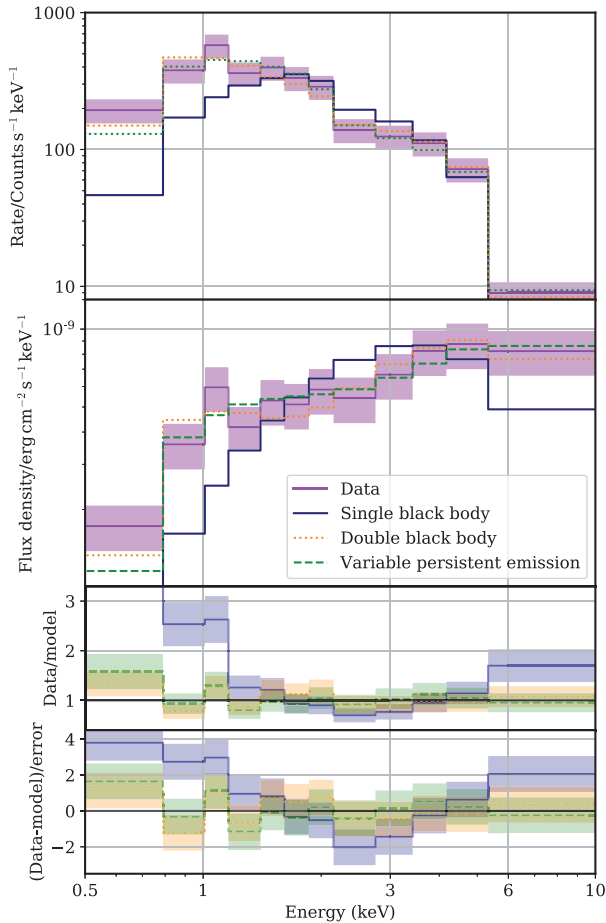
Figure 5. Comparison of different models for the net burst emission at the peak of the burst (the spectrum with the highest count rate in Burst 5). A single blackbody (navy) is a poor fit; two blackbodies (yellow) or a contribution proportional to the persistent flux (green) both give similarly good fits.

persistent emission; we use TBABS × (DISKBB+BBODY), representing an absorbed disc and blackbody (we also use this model for the accretion rate estimates in Section 3.5). This soft state model gives a good fit to the persistent spectra for each burst (the worst case χ^2/dof $= 226.0/212 = 1.066$, $p = 0.24$) and agrees with various properties of the bursts (mentioned throughout this work) which match other bursts observed during the soft state.

Both of these burst models provide good fits to all spectra (Fig. 5) and provide similar peak fluxes and qualitative behaviour of the first blackbody component's radius around the burst peak. The total fit statistics for burst 5 for the spectra from times where a single blackbody gives a poor fit ($\chi^2_\nu > 2$) are: χ^2/dof $= 78.7/76$ for the double blackbody model; and χ^2/dof $= 73.5/83$ when varying the persistent emission. This implies a weak preference for a change in the strength of the persistent component but both models are statistically acceptable so we regard both options as possible. Parameters of the fits of each of these models to burst 5 are shown in Fig. 6. Bursts 2 and 3 show similar features with the lower signal; burst 1 has much lower signal; and we do not analyse burst 4 in detail due to the enhanced background from the SAA.

The area of the blackbody increases around the Type I burst peak before reducing and settling to a steady value for the majority of the burst tail, characteristic of PRE. Both well-fitting models (two blackbodies or additional persistent emission) show a similar degree

of expansion, by around a factor of 2 over the radius in the tail of the burst, once the radius has settled to a steady value. The dip in blackbody radius after the burst peak to below the tail value is typical of bursts while accreting in the soft state, which agrees with our identification from the persistent spectrum, and is likely due to a changing colour-correction factor (Güver, Psaltis & Özel 2012a; Güver, Özel & Psaltis 2012b; Kajava et al. 2014).

These fits show a fast rise and smooth decay in bolometric flux. The apparent double peak in the flux curve for the single blackbody model is likely due to the poor fit around this time, although double peaks in bolometric luminosity have been seen in other PRE bursts (Jaisawal et al. 2019). The comparatively smooth flux profile contrasts with the fast drop in count rate after the peak; the difference being due to the higher temperatures early in the decay producing a lower count rate for a given flux (when convolved with the instrument response, given the *NICER* effective area curve and the temperatures concerned).

Near the times of the Type I burst peaks (within about 2 s), there is an excess of soft emission over the simple blackbody model. Similar excesses have been seen in Type I bursts in many other sources observed with *NICER*, e.g. Aql X-1 (Keek et al. 2018a), 4U 1820–30 (Keek et al. 2018b), and SAX J1808.4–3658 (Bult et al. 2019). This could be due to other extra components such as reemission from the disc (corresponding to the extra blackbody, Keek et al. 2018a) or enhanced accretion through Poynting–Robertson drag (corresponding to the change in persistent emission normalization, Worpel et al. 2013). There may also be a deviation from a simple blackbody due to Comptonization (Keek et al. 2018b) or scattering processes in the atmosphere (Romani 1987). The data for the X-ray bursts presented here are not sensitive enough to distinguish between these possibilities clearly.

3.5 Distance estimate and implications

Since the later Type I bursts (certainly burst 5, with some evidence also in bursts 2 and 3) show PRE, their peak luminosity should be governed by the Eddington limit. The observed flux can then be used to estimate a distance. Initially, we use $L_{\text{Edd}} = 3.79 \times 10^{38}\,\text{erg s}^{-1}$, found empirically by Kuulkers et al. (2003) to be suitable for NSs at known distance, and to have an accuracy of 15 per cent for source-to-source variation. This matches the Eddington limit of a helium atmosphere around a $1.4\,\text{M}_\odot$ object.

We take the peak flux from the second, third and fifth Type I bursts (which are consistent with each other; different temperatures mean that these correspond to different count rates). We use the model of the burst including a scaled persistent emission component (see Section 3.4), although the double blackbody model gives very similar results. For each burst, we use the least-squares average of the fluxes from intervals which are consistent within 1σ of the highest value. These values are consistent with each other and their average is $1.1 \pm 0.1 \times 10^{-8}\,\text{erg cm}^{-2}\,\text{s}^{-1}$, which gives a distance of

$$D = 16.7^{+1.8}_{-1.3}\,\text{kpc}\,(1\sigma).$$

This puts Swift J1858.6–0814 at the far side of the Galaxy; given its Sky coordinates ($l = 26.3894$, $b = -5.3237$), this distance gives a Galactic (cylindrical) radius of 10 kpc and a height of 1.5 kpc below the Galactic plane.

Applying a prior for the relative density of the Galaxy along the line of sight (using the Galaxy model of Dehnen & Binney 1998; Grimm, Gilfanov & Sunyaev 2002; see also Gandhi et al. 2019) reduces this distance slightly, due to the higher density of objects
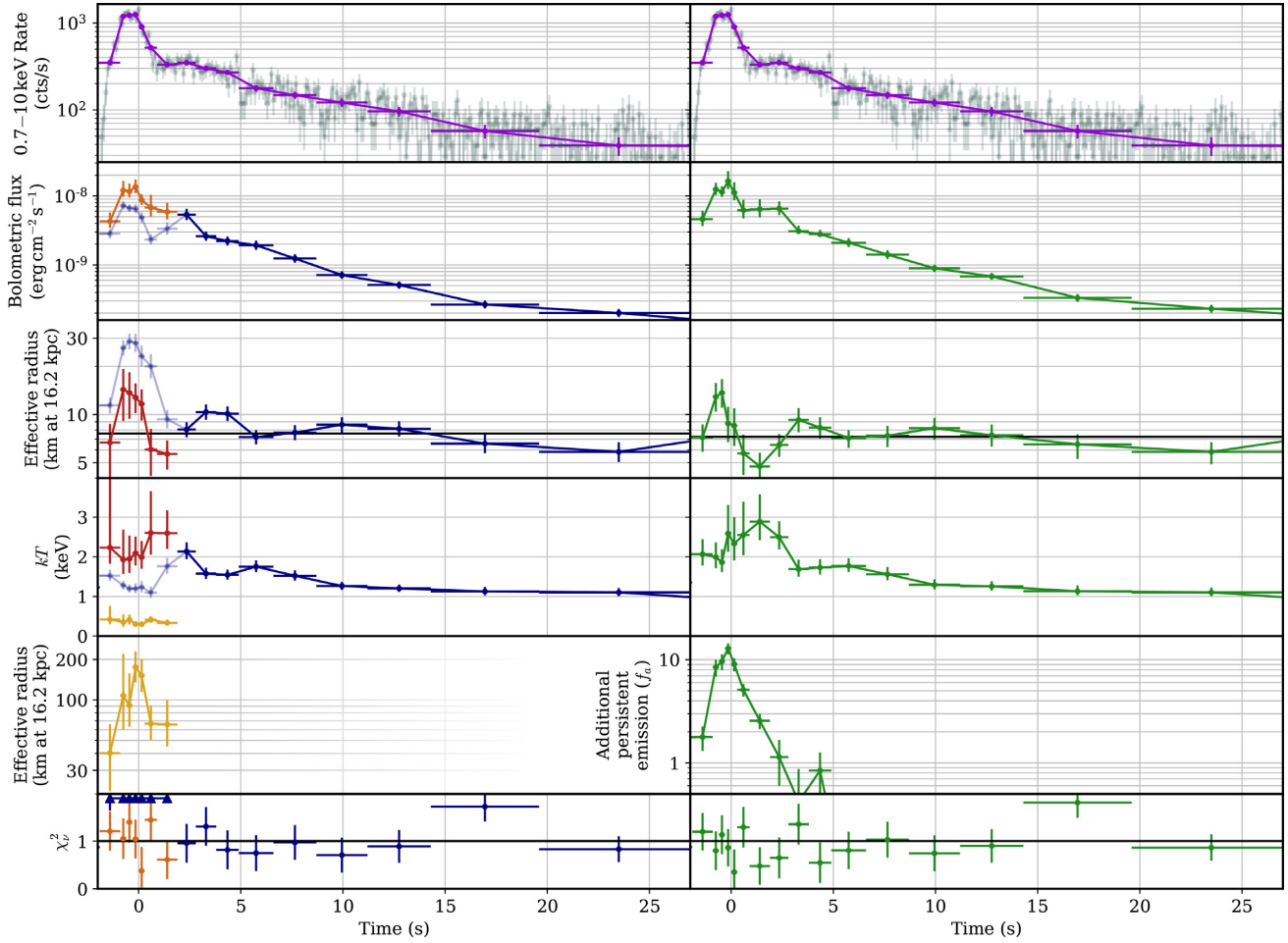
Figure 6. Parameters of time-resolved spectra of Burst 5. Left-hand column: parameters from modelling the Type I burst emission with 1 or 2 blackbodies. Parameters for a single blackbody model are shown in navy; for two blackbodies, values for the complete model are shown in orange; the hotter blackbody in red and the cooler blackbody in yellow. The two-blackbody model is only shown where the single blackbody has $\chi_\nu^2 > 2$ and the single blackbody model is shown in faint navy in these cases. Right-hand column: parameters from modelling the burst with a blackbody and an increase in the normalization of the persistent emission (green). Top panels: light curves at 0.1-s resolution (grey) and binned to the times of the spectra (purple).

closer to the Galactic centre, giving

$$D = 16.2^{+1.5}_{-1.6} \text{ kpc } (1\sigma).$$

From the relative densities of the components of the Galactic model at this position, we infer that Swift J1858.6–0814 is most likely (75 per cent) to be a disc object but could also be part of the halo (25 per cent). A bulge origin is highly unlikely [P(Bulge) = 7×10^{-6}].

There are systematic effects, which may affect this distance estimate (e.g. Galloway, Özel & Psaltis 2008b). Many of these, such as differences in NS mass and photosphere metallicity, are implicitly included by the empirical nature of the critical luminosity (and its uncertainty) measured by Kuulkers et al. (2003). However, the effects of obscuration in high inclination sources are not accounted for – Kuulkers et al. (2003) find that in some high inclination sources the observed PRE luminosity is significantly lower. In this case, the photosphere may be partially obscured by larger components of the system, principally the disc. For the simple case of a razor-thin disc, the disc can obscure up to half of the NS so the flux may be underestimated by up to a factor of 2 and the distance may actually be smaller by a factor of up to $\sqrt{2}$. This factor is mitigated by reflection

of the radiation intercepted by the disc but may be increased by a thick disc (He & Keek 2016).

To show the magnitude of these effects, we show distance estimates for various specific values of metallicity and inclination in Fig. 7 and Table 1. We calculate the distances by replacing the empirical peak luminosity from Kuulkers et al. (2003) with the theoretical Eddington luminosity (e.g. Lewin et al. 1993) modified by the anisotropy factor (ξ_b) from (He & Keek 2016),

$$L_{\text{Obs}} = \frac{8\pi G m_p M_{\text{NS}} c}{\xi_b \sigma_T (1 + X)(1 + z(R))},$$

where G is the gravitational constant, m_p is the proton mass, M_{NS} is the NS mass, c is the speed of light, σ_T is the Thomson cross-section, X is the hydrogen mass fraction, and $z(R)$ is the gravitational redshift at the photospheric radius R. We show the two extremes of likely metallicity, pure helium ($X = 0$) and a cosmic abundance of hydrogen ($X = 0.739$). Since it shows eclipses (Buisson et al. 2020c), Swift J1858.6–0814 is at high inclination; from He & Keek (2016), the appropriate reduction in apparent luminosity (ξ_b^{-1}) for inclinations of 70°–80° is a factor of 0.85–0.65. For each combination of parameters, we show the distance estimate for an NS
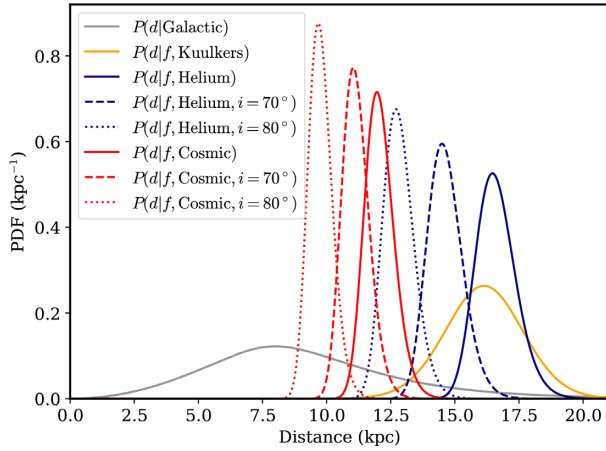
Figure 7. Distance estimates for Swift J1858.6–0814 based on various critical luminosities for PRE. Distance estimates for several specific luminosity values are shown (details in legend and text) along with the empirical luminosity range found by Kuulkers et al. (2003). The Galactic prior is shown in grey.

Table 1. Distance estimates (kpc) for various gas compositions and inclinations (see the text for details).

	Isotropic	$i = 70°$	$i = 80°$
Pure helium	$16.6^{+0.9}_{-0.8}$	$14.6^{+0.8}_{-0.7}$	$12.8^{+0.7}_{-0.6}$
Cosmic abundances	$12.1^{+0.6}_{-0.6}$	$11.1^{+0.6}_{-0.5}$	$9.8^{+0.5}_{-0.4}$

mass of $1.4\,M_\odot$ and a photospheric radius of 20 km. This allows a significantly larger range of distances than the Kuulkers et al. (2003) range, due to the lower effective Eddington luminosities for high hydrogen fractions and high inclination. However, even the smallest distance estimate ($9.8^{+0.5}_{-0.4}$ kpc) is 60 per cent of the value derived from the Kuulkers et al. (2003) luminosity and beyond the average distance of Galactic sources along this line of sight.

To reduce the range of these estimates, we can consider whether particular values of parameters generating the systematic uncertainty are preferred by other evidence. The eclipse duration implies an inclination of at least 70° (Buisson et al., in preparation; Buisson et al. 2020c). A more accurate determination of the inclination would require detailed modelling of optical light curves and spectra, beyond the scope of this paper; meanwhile, we regard our calculation using 80° as a fiducial value. The atmospheric composition of a Type I burst can be inferred from its light curve. The relatively fast rise and initial decay of the PRE bursts observed here suggest a helium burst. Additionally, helium fuelled bursts are also more common during the soft accretion state and the dip in apparent radius below the final value is more typical of soft state bursts (Kajava et al. 2014). Further, bursts can reach the Eddington limit for helium even where accreted material is hydrogen rich, either by the hydrogen being burnt between bursts or the hydrogen-rich atmosphere being blown off by the burst (Galloway et al. 2006; Bult et al. 2019). This would imply that the further distance estimates (blue curves in Fig. 7) are more likely ($12.8^{+0.7}_{-0.6}$ kpc for $i = 80°$).

With this distance estimate, we can also estimate the accretion rate at the times of the bursts from the persistent flux measurements from the modelling in Section 3.5. We find a bolometric (of the X-ray components) flux before the bursts of $12.6^{+0.5}_{-0.4}$, $10.2^{+0.5}_{-0.4}$, $8.9^{+0.6}_{-0.4}$, $5.6^{+0.5}_{-0.3}$,

and $2.3^{+0.2}_{-0.15} \times 10^{-10}$ erg cm^{-2} s^{-1}, in chronological order. If the persistent emission has the same anisotropy as the burst, this implies an Eddington fraction $\dot{m}_{\mathrm{Edd}} = 0.20^{+0.01}_{-0.02}$, $0.16^{+0.01}_{-0.02}$, $0.14^{+0.01}_{-0.02}$, $0.09^{+0.01}_{-0.01}$, and 0.036 ± 0.004 for material in the accretion flow (calculating L_{Edd} for $X = 0.73$). However, the disc and boundary layer may have more anisotropic emission than the burst from the NS surface (e.g. He & Keek 2016), so the true Eddington fraction could be somewhat higher. The exact factor depends on the details of the accretion structure and the inclination; for a flat disc (which provides all the persistent flux) observed at 70°–80°, the increase is by a factor of 1.2–2. This is similar to the range at which helium fuelled bursts are expected and observed (Galloway et al. 2008a) but extends slightly higher, so there could be some influence of residual hydrogen in the burning material.

Our distance estimates are all relatively large (Galloway et al. 2008a; Gandhi et al. 2019) but not unprecedented (e.g. Homan et al. 2014) for an XRB. The absorbing column density ($\approx 2 \times 10^{21}$ cm^{-2}) is comparatively low for such a distant source, but the total Galactic column density in the direction of Swift J1858.6–0814 is similar (1.8×10^{21} cm^{-2}, HI4PI Collaboration et al. 2016).

A large distance can also help in explaining the strong variability observed in the initial state of Swift J1858.6–0814 (during 2018-9): it is comparatively faint for a binary but strong winds (Muñoz-Darias et al. 2020) and variability (Ludlam et al. 2018) are often explained by a high Eddington rate (King & Pounds 2003; Grupe 2004). During the flaring state but between flares, the observed flux of Swift J1858.6–0814 was $\approx 2.5 \times 10^{-10}$ erg cm^{-2} s^{-1} (Hare et al. 2020),[2] which is ≈ 5 per cent of the Eddington limit for hydrogen and a $1.4 M_\odot$ object. Some flares increased count rates by factors of many tens, so at least during bright flares, the luminosity was above the Eddington luminosity (and correcting for any anisotropy is likely only to increase the strength of this). If much of the variability was due to obscuration, the intrinsic luminosity would also have been above Eddington at other times.

3.6 Pre-burst oscillations

We also looked for mHz QPOs, which are sometimes found before an X-ray burst (e.g. Revnivtsev et al. 2001; Altamirano et al. 2008; Mancuso et al. 2019). We used 0.5–10 keV light curves at 1-s resolution and applied the Lomb–Scargle periodogram (Lomb 1976; Scargle 1982) to each gapless light curve, excluding periods of dipping and eclipses. In the five cases, where we detected the type-I X-ray bursts, we searched for the oscillations before and after the X-ray bursts. To estimate the significance level, we followed the approach of Press et al. (1992), which assumes white noise and takes as a number of trials the number of frequencies explored.

We detected an mHz QPO at a significance of 5.8σ in the 1.8 ks of data before the 5th X-ray burst (Fig. 8). The mHz QPO has an average frequency of 9.6 ± 0.5 mHz and a fractional rms amplitude of 2.2 ± 0.2 per cent (0.5–10 keV). There is no evidence of the oscillations in the ≈ 600 s of data after the X-ray burst, with a 90 per cent upper limit on the rms amplitude of 1.2 per cent ruling out that the same strength of oscillation continues. We also found marginal evidence of QPOs in at least three other cases; however, the data sets are relatively short ($\lesssim 500$–700 s), and therefore it is not possible to understand if they are real or the product of red noise. The upper limits to the QPO amplitude for the time segments prior

---

[2]This was measured for the 3-78 keV band, which for the spectral shape of this observation includes the majority of flux; any bolometric correction will only increase the strength of super-Eddington behaviour.
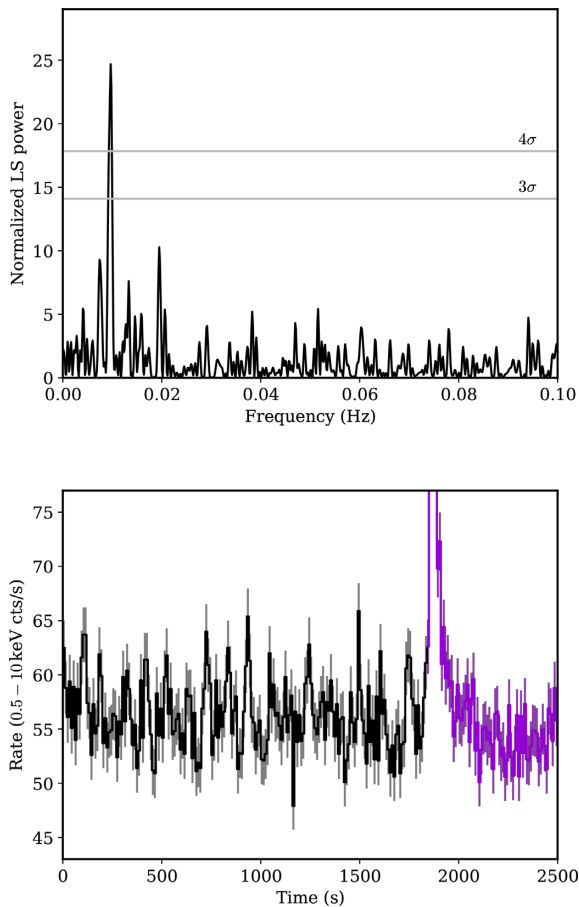
Figure 8. Top panel: Lomb–Scargle periodogram of the light curve segment immediately prior to burst 5, which shows a QPO at 9.6 ± 0.5 mHz. Bottom panel: 0.5–10 keV *NICER* light curve of the period up to and including burst 5, during which a 9.6 ± 0.5 mHz QPO is detected. The burst itself (purple) far exceeds the plotted range.

to the earlier bursts are somewhat lower in fractional amplitude (0.6, 0.8, 1.0, and 0.8 per cent in chronological order) than for the detected QPO but due to the brighter flux at earlier times, all but the last of these limits are higher in absolute amplitude than the detected QPO. Therefore, we cannot definitively rule out a QPO from the same level of oscillatory burning occurring prior to the other bursts. We also note that an mHz QPO was also detected in a *NuSTAR* observation during 2019 February (Hare et al. 2019), although at a frequency of 2.7 mHz, which is lower than other mHz QPOs which have been explained by marginally stable nuclear burning.

Revnivtsev et al. (2001) find that these mHz QPOs are only found in a narrow range of luminosities, $L_{3-20 \, keV} = 5 - 11 \times 10^{36} \, erg \, s^{-1}$. The QPO found here occurs while the mean flux (from our model for the persistent emission, Section 3.4) is $f_{3-20 \, keV} = 1.4 \pm 0.2 \times 10^{10} \, erg \, cm^{-2} \, s^{-1}$, which corresponds to $L_{3-20 \, keV} = 4.3^{+0.6}_{-0.5} \times 10^{36} \, erg \, s^{-1}$ at 16.2 kpc (derived from the Type I burst peak luminosity for the population, since we are comparing with a population luminosity for other QPO detections), which supports the upper end of the distance estimates found here. Using a lower distance to account for the effect of high inclination in Swift J1858.6–0814 would imply a lower luminosity, which is compatible with the luminosities at which QPOs are observed in other sources if this also depends on inclination, with at least as strong an anisotropy factor as

the burst emission. This would be expected for disc, NS surface or coronal emission so long as this is not strongly equatorially beamed.

The characteristics of the mHz QPOs we found here are consistent with those found in 6 other NS systems (but compare Linares et al. 2012 Revnivtsev et al. 2001; Altamirano et al. 2008; Strohmayer & Smith 2011; Lyu, Méndez & Altamirano 2014; Lyu et al. 2015; Strohmayer et al. 2018; Mancuso et al. 2019) and are usually explained as being the product of marginally stable burning of He on the NS surface (Heger et al. 2007). This is the seventh NS system that shows this type of QPOs. The fact that we do not detect more episodes of mHz QPOs could either be due to their intrinsic absence or to detection difficulty: the mHz QPOs are not always present in the X-ray light curves (they are state-dependent and even in a given state, there is not yet a clear physical trigger for them, see Altamirano et al. 2008; Mancuso et al. 2019, etc.); in addition, the frequency and amplitude of these QPOs are very low, and therefore to acquire enough QPO cycles and sufficient signal-to-noise ratio, uninterrupted data sets longer than 1000–1500 s are generally needed to unambiguously detect them.

3.7 Burst oscillation search

We searched each of the X-ray bursts observed with *NICER* for the presence of burst oscillations, but did not detect any significant signals. To search for oscillations, we constructed a 1/8192 s time-resolution light curve for each X-ray burst, using only those events in the 1–8 keV energy band. These light curves all started 10 s prior to the burst onset, and had durations of 40 s. For each considered X-ray burst, we applied a $T = 2, 4, 8$ s duration window selection, which we moved across the burst profile in steps of $T/2$. We then calculated the power spectrum associated with each window position, and searched the 100–2000 Hz frequency range for excess power over the expected noise distribution. No such excess was observed, to a 95 per cent confidence upper limit of approximately 15 per cent fractional amplitude in the most sensitive segment (the peak light curve of burst 5). We note, however, that the vast majority of considered segments had much lower averaged count rates, and thus substantially higher upperlimits. With typical upper limits ranging between 30 and 80 per cent fractional amplitude, our results are therefore not especially constraining.

4 FURTHER DISCUSSION

4.1 Implications of the NS accretor

The identification of the accretor in Swift J1858.6–0814 as an NS informs several outstanding questions relating to the properties of Swift J1858.6–0814. It fits with the low coronal temperature found in Hare et al. (2020), since NSs tend to have lower coronal temperatures than BHs (Burke et al. 2017).

However, the NS accretor implies an unusual location in the radio-X-ray plane: Swift J1858.6–0814 appears relatively X-ray faint for a NS XRB (van den Eijnden et al. 2020). This could imply that Swift J1858.6–0814 has an intrinsically unusually low X-ray/radio luminosity ratio or that the observed X-ray luminosity is unrepresentatively low. The latter case would support a model in which the X-ray emission (which may already be comparatively low due to anisotropy, e..g He & Keek 2016) is usually obscured by the high inclination disc, apart from during the flares, which represent the true intrinsic luminosity, when viewing the central source directly through a gap in the (irregular) disc surface.

Swift J1858.6–0814 has previously been compared with the BH XRBs V4641 Sgr and V404 Cyg (e.g. Hare et al. 2020). All of these sources have shown strong variability due to some combination of changes in intrinsic flux and obscuration, although the relative contribution of these two effects is not yet clear (e.g. compare Walton et al. 2017; Koljonen & Tomsick 2020). The relative radio loudness also provides a further similarity with V404 Cyg, which is unusually radio-loud for its inclination (Motta, Casella & Fender 2018). The identification of Swift J1858.6–0814 as an NS XRB means the flaring behaviour in these sources must now be explained in a model which is compatible with an NS accretor. In particular, extreme variability from processes very close to the event horizon may be ruled out, since an NS is significantly larger than its Schwarzschild radius.

4.2 Bursts in the flaring state?

Swift J1858.6–0814 had been active for over a year before any Type I bursts were detected; there are several means to explain the non-detection of bursts during this period. First, there may truly have been no bursts, due to the different accretion regime during this period. In a model, where variable obscuration causes much of the strong variability, the intrinsic accretion rate was much higher during the flaring period, so would likely have induced stable nuclear burning of both hydrogen and helium. Additionally, in this model, the obscuration between flares would have impeded observation of any Type I bursts which occurred while the NS was obscured (which is the majority of the duty cycle). It is also possible that bursts were observed but not identified if they occurred at the same time as flares. The observed flares are all different in spectrum, light curve and/or duration to thermonuclear bursts; however, the variety of flares means that it is possible that a burst coincident with a flare would go unnoticed. Finally, it is also possible that bursts did occur during this phase of the outburst but, by chance, not during *NICER* observations of Swift J1858.6–0814. Overall, it is unsurprising that X-ray bursts had not been detected in the flaring state, whether or not they occurred.

4.3 Comparison with other similar sources

We can also compare the flaring state to other strong variability regimes in NSs. Two famous NS systems exhibiting flare-like behaviour are the Rapid Burster (MXB 1730–335, e.g. Hoffman et al. 1978) and Bursting Pulsar (GRO J1744–28, Fishman et al. 1995). The Rapid Burster shows many (up to thousands per day) 'rapid' bursts in addition to Type I bursts; these rapid bursts are much shorter ($<10\,\mathrm{s}$) and more regular in cadence than the flares of Swift J1858.6–0814, so are probably different phenomena. The Bursting Pulsar is the archetypal example of Type II X-ray bursts (Kouveliotou et al. 1996). These bursts also differ markedly from the flares observed in Swift J1858.6–0814: The type II bursts are again much shorter and are accompanied by a drop in emission following the burst. Therefore, the flaring state of Swift J1858.6–0814 is not explained as an example of these other unusual NS XRB states.

The high inclination NS LMXB EXO 0748–676 has also shown flaring episodes (Homan, Wijnands & van den Berg 2003), although these are more sporadically interspersed with other light-curve shapes and less prominent at harder energies than those in Swift J1858.6–0814.

Transitional millisecond pulsars (tMSPs) also have a 'flaring' accretion mode (de Martino et al. 2013; Bogdanov & Halpern 2015), although this occurs at much lower luminosity ($\approx 10^{34}\,\mathrm{erg\,s^{-1}}$) than the flaring state in Swift J1858.6–0814 ($\gtrsim 10^{36}\,\mathrm{erg\,s^{-1}}$ observed).

The tMSP flaring mode can also show strong, variable absorption (e.g. Li et al. 2020), so could be an analogue with lower accretion efficiency.

There have not yet been measurements of the magnetic field strength in Swift J1858.6–0814; the closer comparison of the flaring state of Swift J1858.6–0814 with BH than NS systems could be because the magnetic field of its NS is low enough to be unimportant in its accretion flow, implying a relatively low magnetic field strength.

DATA AVAILABILITY

The data underlying this paper are available in HEASARC.

REFERENCES

Altamirano D., van der Klis M., Wijnands R., Cumming A., 2008, ApJ, 673, L35
Arzoumanian Z. et al., 2014, Proc. SPIE, 9144, 914420
Bildsten L., 1995, ApJ, 438, 852
Bildsten L., 1998, in Buccheri R., van Paradijs J., Alpar A., eds, NATO Advanced Science Institutes (ASI) Series C Vol. 515, NATO Advanced Science Institutes (ASI) Series C. Kluwer, Dordrecht, p. 419
Bogdanov S., Halpern J. P., 2015, ApJ, 803, L27
Bolton C. T., 1972, Nat. Phys. Sci., 240, 124
Brown E. F., Bildsten L., Rutledge R. E., 1998, ApJ, 504, L95
Buisson D. J. K. et al., 2020a, MNRAS, 498, 68
Buisson D. J. K. et al., 2020c, Astron. Telegram, 13563, 1
Buisson D. J. K., Altamirano D., Remillard R., Arzoumanian Z., Gendreau K., Gandhi P., Vincentelli F., 2020b, Astron. Telegram, 13536, 1

Bult P. et al., 2019, ApJ, 885, L1

Burke M. J., Gilfanov M., Sunyaev R., 2017, MNRAS, 466, 194

Casares J., Charles P. A., Naylor T., 1992, Nature, 355, 614

Cornelisse R., Heise J., Kuulkers E., Verbunt F., in't Zand J. J. M., 2000, A&A, 357, L21

Cumming A., Bildsten L., 2001, ApJ, 559, L127

Cumming A., Macbeth J., 2004, ApJ, 603, L37

de Martino D. et al., 2013, A&A, 550, A89

Dehnen W., Binney J., 1998, MNRAS, 294, 429

Fishman G. J., Kouveliotou C., van Paradijs J., Harmon B. A., Paciesas W. S., Briggs M. S., Kommers J., Lewin W. H. G., 1995, IAU Circ., 6272, 1

Fujimoto M. Y., Hanawa T., Miyaji S., 1981, ApJ, 247, 267

Gallo E., Degenaar N., van den Eijnden J., 2018, MNRAS, 478, L132

Galloway D. K. et al., 2018, ApJ, 857, L24

Galloway D. K., Keek L., 2017, preprint (arXiv:1712.06227)

Galloway D. K., Cumming A., Kuulkers E., Bildsten L., Chakrabarty D., Rothschild R. E., 2004, ApJ, 601, 466

Galloway D. K., Psaltis D., Muno M. P., Chakrabarty D., 2006, ApJ, 639, 1033

Galloway D. K., Muno M. P., Hartman J. M., Psaltis D., Chakrabarty D., 2008a, ApJS, 179, 360

Galloway D. K., Özel F., Psaltis D., 2008b, MNRAS, 387, 268

Gandhi P. et al., 2016, MNRAS, 459, 554

Gandhi P., Rao A., Johnson M. A. C., Paice J. A., Maccarone T. J., 2019, MNRAS, 485, 2642

Gendreau K. C. et al., 2016, Proc. SPIE, 9905, 99051H

Gottwald M., Haberl F., Parmar A. N., White N. E., 1986, ApJ, 308, 213

Grimm H. J., Gilfanov M., Sunyaev R., 2002, A&A, 391, 923

Grindlay J., Gursky H., Schnopper H., Parsignault D. R., Heise J., Brinkman A. C., Schrijver J., 1976, ApJ, 205, L127

Grupe D., 2004, AJ, 127, 1799

Güver T., Psaltis D., Özel F., 2012a, ApJ, 747, 76

Güver T., Özel F., Psaltis D., 2012b, ApJ, 747, 77

Hare J. et al., 2020, ApJ, 639, 103

Hare J., Gandhi P., Paice J. A., Tomsick J., 2019, Astron. Telegram, 12512, 1

Harrison F. A. et al., 2013, ApJ, 890, 12

He C. C., Keek L., 2016, ApJ, 819, 47

Heger A., Cumming A., Woosley S. E., 2007, ApJ, 665, 1311

Hewish A., Bell S. J., Pilkington J. D. H., Scott P. F., Collins R. A., 1968, Nature, 217, 709

HI4PI Collaboration et al., 2016, A&A, 594, A116

Hoffman J. A., Marshall H. L., Lewin W. H. G., 1978, Nature, 271, 630

Homan J., Wijnands R., van den Berg M., 2003, A&A, 412, 799

Homan J., Fridriksson J. K., Wijnands R., Cackett E. M., Degenaar N., Linares M., Lin D., Remillard R. A., 2014, ApJ, 795, 131

in't Zand J., 2017, in Serino M., Shidatsu M., Iwakiri W., Mihara T., eds, 7 years of MAXI: monitoring X-ray Transients. RIKEN, Saitama, Japan, p. 121

Jaisawal G. K. et al., 2019, ApJ, 883, 61

Kajava J. J. E. et al., 2014, MNRAS, 445, 4218

Keek L. et al., 2018a, ApJ, 855, L4

Keek L. et al., 2018b, ApJ, 856, L37

Keek L., Heger A., in't Zand J. J. M., 2012, ApJ, 752, 150

Kennea J. A., Krimm H. A., 2018, Astron. Telegram, 12160, 1

King A. R., Pounds K. A., 2003, MNRAS, 345, 657

Koljonen K. I. I., Tomsick J. A., 2020, A&A, 639, 23

Kouveliotou C., van Paradijs J., Fishman G. J., Briggs M. S., Kommers J., Harmon B. A., Meegan C. A., Lewin W. H. G., 1996, Nature, 379, 799

Krimm H. A. et al., 2018, Astron. Telegram, 12151, 1

Kuulkers E., den Hartog P. R., in't Zand J. J. M., Verbunt F. W. M., Harris W. E., Cocchi M., 2003, A&A, 399, 663

Lewin W. H. G., Vacca W. D., Basinska E. M., 1984, ApJ, 277, L57

Lewin W. H. G., van Paradijs J., Taam R. E., 1993, Space Sci. Rev., 62, 223

Li K.-L., Strader J., Miller-Jones J. C. A., Heinke C. O., Chomiuk L., 2020, ApJ, 895, 16

Linares M., Altamirano D., Chakrabarty D., Cumming A., Keek L., 2012, ApJ, 748, 82

Lomb N. R., 1976, Ap&SS, 39, 447

Ludlam R. M. et al., 2018, Astron. Telegram, 12158, 1

Lyu M., Méndez M., Altamirano D., 2014, MNRAS, 445, 3659

Lyu M., Méndez M., Zhang G., Keek L., 2015, MNRAS, 454, 541

Lyu M., Méndez M., Altamirano D., Zhang G., 2016, MNRAS, 463, 2358

McClintock J. E., Remillard R. A., 2006, in Lewin W., van der Klis M., eds, Black Hole Binaries. Cambridge Univ. Press, Cambridge, p. 157

Mancuso G. C., Altamirano D., García F., Lyu M., Méndez M., Combi J. A., Díaz-Trigo M., in't Zand J. J. M., 2019, MNRAS, 486, L74

Migliari S., Fender R. P., 2006, MNRAS, 366, 79

Motta S. E., Kajava J. J. E., Sánchez-Fernández C., Giustini M., Kuulkers E., 2017, MNRAS, 468, 981

Motta S. E., Casella P., Fender R. P., 2018, MNRAS, 478, 5159

Muñoz-Darias T. et al., 2020, ApJ, 893, L7

Munoz-Darias T., Jimenez-Ibarra F., Armas Padilla M., Casares J., Cuneo V., Panizo-Espinar G., Sanchez-Sierras J., Torres M. A. P., 2019, Astron. Telegram, 12881, 1

Narayan R., Heyl J. S., 2003, ApJ, 599, 419

Orosz J. A. et al., 2001, ApJ, 555, 489

Orosz J. A., Bailyn C. D., 1997, ApJ, 477, 876

Paice J. A., Gandhi P., Dhillon V. S., Marsh T. R., Green M., Breedt E., 2018, Astron. Telegram, 12197, 1

Patruno A., Watts A. L., 2012, preprint (arXiv:1206.2727)

Press W. H., Teukolsky S. A., Vetterling W. T., Flannery B. P., 1992, Numerical recipes in FORTRAN: The Art of Scientific Computing, 2nd ed. Cambridge: Univ. Press, Cambridge

Revnivtsev M., Churazov E., Gilfanov M., Sunyaev R., 2001, A&A, 372, 138

Revnivtsev M., Gilfanov M., Churazov E., Sunyaev R., 2002, A&A, 391, 1013

Reynolds M. T., Miller J. M., Ludlam R. M., Tetarenko B. E., 2018, Astron. Telegram, 12220, 1

Romani R. W., 1987, ApJ, 313, 718

Scargle J. D., 1982, ApJ, 263, 835

Spitkovsky A., Levin Y., Ushomirsky G., 2002, ApJ, 566, 1018

Strohmayer T. E. et al., 2018, ApJ, 865, 63

Strohmayer T., Bildsten L., 2006, in Lewin W., van der Klis M., eds, New Views of Thermonuclear Bursts. Cambridge Univ. Press, Cambridge, p. 113

Strohmayer T. E., Brown E. F., 2002, ApJ, 566, 1045

Strohmayer T. E., Smith E. A., 2011, Astron. Telegram, 3258, 1

Strohmayer T. E., Zhang W., Swank J. H., Smale A., Titarchuk L., Day C., Lee U., 1996, ApJ, 469, L9

Tawara Y. et al., 1984, ApJ, 276, L41

van den Eijnden J. et al., 2020, MNRAS, 496, 4127

van der Klis M., 1994, ApJS, 92, 511

van der Klis M., 2006, in Lewin W., van der Klis M., eds, Rapid X-ray Variability. Cambridge Univ. Press, Cambridge, p. 39

van der Klis M., Swank J. H., Zhang W., Jahoda K., Morgan E. H., Lewin W. H. G., Vaughan B., van Paradijs J., 1996, ApJ, 469, L1

van Paradijs J., 1978, Nature, 274, 650

Walton D. J. et al., 2017, ApJ, 839, 110

Webster B. L., Murdin P., 1972, Nature, 235, 37

Wijnands R., van der Klis M., 2000, ApJ, 528, L93

Worpel H., Galloway D. K., Price D. J., 2013, ApJ, 772, 94

Zdziarski A. A., Lubiński P., Smith D. A., 1999, MNRAS, 303, L11

APPENDIX: SUMMARY OF BURST PROPERTIES

Table A1. Summary of burst properties.

Burst number	Recurrence time[a] (d)	Peak rate[b] (0.7–10 keV counts s^{-1})	Persistent flux[c] ($\times 10^{-10}$ erg cm^{-2} s^{-1})	Persistent accretion rate[d] ($\dot{M}_{\rm Edd}$)	mHz QPO frequency[e] (mHz)	mHz QPO amplitude[e]
1	–	550 ± 75	$12.6^{+0.5}_{-0.4}$	$0.20^{+0.01}_{-0.02}$	–	<0.6%
2	≤4.5	960 ± 100	$10.2^{+0.5}_{-0.4}$	$0.16^{+0.01}_{-0.02}$	–	<0.8%
3	≤3.6	1190 ± 110	$8.9^{+0.6}_{-0.4}$	$0.14^{+0.01}_{-0.02}$	–	<1.0%
4	≤6.3	740 ± 90	$5.6^{+0.5}_{-0.3}$	$0.09^{+0.01}_{-0.01}$	–	<0.8%
5	≤1.4	1490 ± 120	$2.3^{+0.2}_{-0.15}$	0.036 ± 0.004	9.6 ± 0.5	2.2 ± 0.2%

Notes. [a]Recurrence times are upper limits as bursts may have occurred between observations. [b]Peak rate is the highest value in the 0.7–10 keV light curve binned to 0.1 s. [c]Persistent flux is measured bolometrically. [d]The persistent accretion rate is not corrected for the effects of anisotropy, which likely increase it by a factor of 1.2–2. [e]The mHz QPO is measured over 0.5–10 keV.

[1]*Department of Physics and Astronomy, University of Southampton, High-field, Southampton SO17 1BJ, UK*

[2]*Department of Astronomy, University of Maryland, College Park, MD 20742, USA*

[3]*NASA/Goddard Space Flight Center, Code 662, Greenbelt, MD 20771, USA*

[4]*Instituto Argentino de Radioastronomía(CCT-La Plata, CONICET; CICPBA), C.C. No. 5, 1894 Villa Elisa, Argentina*

[5]*Facultad de Ciencias Astronómicas y Geofísicas, Universidad Nacional de La Plata, Paseo del Bosque s/n, 1900 La Plata, Argentina*

[6]*Istanbul University, Science Faculty, Department of Astronomy and Space Sciences, Beyazıt, 34119 Istanbul, Turkey*

[7]*Istanbul University Observatory Research and Application Center, Istanbul University, 34119 Istanbul Turkey*

[8]*National Space Institute, Technical University of Denmark, Elektrovej 327-328, DK-2800 Lyngby, Denmark*

[9]*MIT Kavli Institute for Astrophysics and Space Research, Massachusetts Institute of Technology, Cambridge, MA 02139, USA*

[10]*IRAP, CNRS, UPS, CNES, 9 avenue du Colonel Roche, BP 44346, F-31028 Toulouse Cedex 4, France*

[11]*Eureka Scientific, Inc., 2452 Delmer Street, Oakland, CA 94602, USA*

[12]*SRON, Netherlands Institute for Space Research, Sorbonnelaan 2, NL-3584 CA Utrecht, The Netherlands*

[13]*Department of Astronomy, Tsinghua University, Shuangqing Road 30, Beijing 100084, China*

[14]*Tsinghua Center for Astrophysics, Tsinghua University, Shuangqing Road 30, Beijing 100084, China*

[15]*NASA Marshall Space Flight Center, NSSTC, 320 Sparkman Drive, Huntsville, AL 35805, USA*

[16]*Universities Space Research Association, Science and Technology Institute, 320 Sparkman Drive, Huntsville, AL 35805, USA*

[17]*Department of Astronomy, University of Michigan, 1085 South University Avenue, Ann Arbor, MI 48109-1104, USA*

[18]*Department of Astronomy & Astrophysics, Atatürk University, 25240 Erzurum, Turkey*

[19]*Astrophysics Science Division and Joint Space-Science Institute, NASA's Goddard Space Flight Center, Greenbelt, MD 20771, USA*

[20]*Department of Physics, Tor Vergata University of Rome, Via della Ricerca Scientifica 1, I-00133 Rome, Italy*

[21]*INAF –Astronomical Observatory of Rome, Via Frascati 33, I-00078 Monte Porzio Catone (Rome), Italy*

[22]*Space Sciences Laboratory, 7 Gauss Way, University of California, Berkeley, CA 94720-7450, USA*

[23]*Institute of Astronomy, Madingley Road, Cambridge CB3 0HA, UK*

This paper has been typeset from a TEX/LATEX file prepared by the author.